RESEARCH PAPER

Phase-field simulation of impingement and spreading of micro-sized droplet on heterogeneous surface

Chun Yee Lim · Yee Cheong Lam

Abstract A numerical investigation on the impingement and spreading of a micro-sized droplet with nonzero impact velocities on a surface with heterogeneous wettability is presented in this paper. The numerical model was implemented through phase-field simulation with finite element formulation. A simple scheme based on interfacial phase-field function gradient was proposed to track the velocity of contact line which was required to specify the dynamic contact angle based on hydrodynamic theory and molecular kinetic approach. For a circular pattern with a higher wettability than the surrounding surface, the impinging droplet final spread diameter decreases with an increasing wettability contrast. The droplet conforms to the circular patterns with smaller diameters up to a threshold, which is dictated by the wettability of the surface surrounding the pattern. Impact velocity of the droplet affects the maximum spread diameter but not the final conformability to a wettability pattern. Impingement and anisotropic spreading of a droplet on a stripe pattern was also demonstrated in a three-dimensional simulation. The high wettability contrast between the inner and outer regions of the stripe pattern confines droplet spreading and elongates the droplet in the direction of the stripe. These simulations demonstrated the conditions for a jetted micro-sized droplet to be confined to a specific area through wettability patterning, which can potentially improve the precision of current inkjet printing technology.

C. Y. Lim · Y. C. Lam (✉)
School of Mechanical and Aerospace Engineering,
Nanyang Technological University, 50 Nanyang Avenue,
Singapore 639798, Singapore
e-mail: myclam@ntu.edu.sg

List of symbols

Ca_s	Spreading capillary number
Cn	Cahn number
D	Initial diameter of droplet (m)
D^*	Dimensionless droplet spread diameter
D_h	Diameter of circular pattern (m)
D_h^*	Dimensionless diameter of circular pattern
Fr	Froude number
f_o	Characteristic frequency of molecular displacement (Hz)
f_o^s	Equilibrium frequency of molecular displacement when retarded only by solid–liquid interaction (Hz)
f_ε	Defect force per unit length (N m^{-1})
G	Chemical potential (Pa)
g	Gravitational acceleration (m s^{-2})
$\mathbf{g}$	Gravitational acceleration vector (m s^{-2})
$\mathbf{g}^*$	Dimensionless gravitational acceleration vector
H	Droplet height (m)
H^*	Dimensionless droplet height
h	Planck constant (m^2 kg s^{-1})
k_b	Boltzmann constant (m^2 kg s^{-2} K^{-1})
L	Macroscopic characteristic length (m)
L_m	Microscopic characteristic length (m)
$\mathbf{n}$	Normal vector to surface
Pe	Peclet number
p	Pressure (Pa)
p^*	Dimensionless pressure
Re	Reynolds number
r	Radial displacement (m)
T	Temperature (K)
t	Time (s)

t^*	Dimensionless time
U	Initial/impact velocity of droplet (m s^{-1})
u	Velocity vector (m s^{-1})
u*	Dimensionless velocity vector
V_f	Volume fraction of liquid
v_{cl}	Contact-line velocity (m s^{-1})
v_m	Molecular flow volume (m^3)
We	Weber number
β	Friction parameter (kg m^{-1} s^{-1})
γ_1	Interfacial tension between solid and liquid (N m^{-1})
γ_2	Interfacial tension between solid and air (N m^{-1})
$\Delta\sigma_o$	Constant component for interfacial tension difference (N m^{-1})
ε	Interfacial thickness (m)
θ_a	Apparent contact angle
θ_m	Microscopic contact angle
θ_s	Static contact angle
θ_{s1}	Static contact angle inside circular pattern
κ	Phase-field mobility (m^3 s kg^{-1})
λ	Molecular displacement length (m)
λ_m	Mixing energy density (N)
μ	Dynamic viscosity (Pa s)
μ_e	Equivalent dynamic viscosity for two fluids (Pa s)
ρ	Density (kg m^{-3})
σ	Surface tension (N m^{-1})
ϕ	Phase-field function
ψ	Intermediate variable in Cahn–Hilliard equation

1 Introduction

Inkjet printing technology has found numerous applications since its original application of printing digital images or text on papers. In recent years, inkjet technology has been employed to deposit functional materials which are mixed with liquid, directly on a solid substrate. Example applications of inkjet printing include manufacturing of light-emitting diode (LED) display panel (Haskal et al. 2002; Koo et al. 2006; Ummartyotin et al. 2011), plastic transistor circuits (Sirringhaus et al. 2000), three-dimensional electronic circuits (Mei et al. 2005) and DNA micro-arrays (Heller 2002; Kumar et al. 2005). Impingement and spreading of a droplet on a solid substrate are the critical processes that determine the size and location of the features to be deposited.

Conventional inkjet material deposition for the creation of micron-sized feature is limited to a minimum of 20–50 μm (Sele et al. 2005) because of the difficulties in generating smaller droplet and controlling of droplet spreading. However, manufacturing of electronic devices such as field-effect transistors (FET) or active matrix display with thin-film transistor (TFT) circuit often demands highly accurate deposition of smaller feature (Tekin et al. 2008; Arias et al.

2004). A jetted droplet will also spread beyond its static diameter upon impingement and might contaminate adjacent droplets which are deposited at close proximity, for example, on a DNA micro-array. Among the solutions to overcome these problems, small grooves with width ranging from 5 to 15 μm have been embossed on the surface to guide the spreading of droplet (Hendriks et al. 2008). Surface energy patterning (to create hydrophobic and hydrophilic regions) has also been exploited to fabricate 15 μm to 500 nm features through the dewetting of droplets and preventing uncontrollable spreading of ink droplets on substrates (Sirringhaus et al. 2000; Wang et al. 2004; Lin et al. 2009). Droplet movement driven by heterogeneity in wettability (Bliznyuk et al. 2011; Chaudhury and Whitesides 1992; Kooij et al. 2012; Chu et al. 2010) has also been demonstrated and could be utilized as a potential mechanism to align and position droplet on the substrate. In this investigation, we focus on the spreading of an impinging droplet with a finite velocity on a surface with heterogeneous wettability. We assume that the wetted surface is smooth (roughness is small as compared to the size of the droplet).

To understand the spreading of droplets on a heterogeneous surface, various experimental and theoretical studies have been performed. Wenzel (1936) and Cassie and Baxter (1944) are among the first few researchers who presented the classical studies on the wetting of a sessile droplet on a heterogeneous surface. Further studies of three-phase contact-line dynamics on heterogeneous surfaces have been conducted for the dipping of a plate into a liquid bath (Joanny and Robbins 1990) and liquid column in a capillary tube (Raphael and de Gennes 1989). Léopoldès and Bucknall (2005) experimentally showed that, on a micro-stripe surface with high wettability contrast, a droplet spreads mainly along the stripe pattern direction, while the contact line is pinned in the perpendicular direction, resulting in an elongated droplet. In these experimental investigations, the droplet size is one to two order larger than the width of the stripe and the spreading behavior was shown to be dependent on the relative width of the hydrophilic and hydrophobic strips (Bliznyuk et al. 2009). Bliznyuk et al. (2010) also identified the two spreading regimes on a heterogeneous surface, namely the inertial regime where the droplet is only affected weakly by surface heterogeneity and the capillary regime where the droplet interacts with the surface heterogeneity.

Previous numerical and experimental studies typically allow the droplet to span over multiple heterogeneous stripes because the droplet size is much larger than the width of the micro-sized strips (Xia et al. 2012; Kooij et al. 2012; Jansen et al. 2012). These investigations highlighted the use of the multi-stripe pattern to elongate and move a droplet in a certain direction. However, accurate positioning of a jetted droplet on a specific location and its wettability pattern have

not been investigated. The possible interference between adjacent droplets after impingement on a heterogeneous surface during the printing of densely packed features has also not been examined in the literature.

Numerous numerical simulations (Brandon et al. 1997; Schwartz and Eley 1998; Kusumaatmaja and Yeomans 2007; Kusumaatmaja et al. 2008) of spontaneous spreading of a partially wetting sessile droplet on a heterogeneous surface have also been performed. These studies focus on the spreading behavior of a sessile semi-spherical droplet or a spherical droplet which is initially in contact with the surface. However, numerical studies which consider a droplet traveling at a finite (nonzero) velocity before impingement typically assume a homogeneous surface (Yokoi et al. 2009; Lee and Liu 2010; Briones et al. 2010; Ganesan 2013). Recent numerical studies on droplet spreading and impingement are summarized in Table 1 with the corresponding Weber number *We* (which shows the ratio of impact inertia to surface tension) to highlight the novelty of our numerical investigation. Hitherto, simulations for a micro-droplet traveling at a finite velocity and impinging on a heterogeneous surface are lacking in the literature. Our studies extend the existing studies by focusing on the droplet impact and spreading behaviors on surfaces with heterogeneous wettability under a finite *We* or nonzero impact velocity. The spreading behaviors, i.e., evolution of contact angle, aspect ratio and equilibrium shape of the droplet, have been experimentally shown to differ between jetting a droplet on the surface and depositing the droplet slowly on a similar surface (Jansen et al. 2012). The behaviors of droplets under these conditions have practical implications such as inkjet printing with feature dimensions less than the droplet diameter. Unique behaviors, specifically the interaction of such droplet with wettability contrast and conformability of the droplet to the wettability pattern, are investigated in detail in our studies.

This investigation presents a numerical study of a micro-sized droplet impinging and spreading on a circular or stripe pattern with wettability contrast to the surrounding surface. The circular pattern is chosen for ease of analysis arising from its axisymmetry, while the rectangular stripe pattern is examined because of its application in the fabrication of FET, TFT and other electronic circuits. The outcome of this study can be applied to confine a jetted droplet to a specific area and control the spreading dynamics of the droplet upon impingement to prevent interference with adjacent droplets.

2 Numerical simulation

Droplet impingement and spreading have been simulated with various numerical models, for example, level-set method, volume of fluid, phase-field method, lattice Boltzmann method and arbitrary Lagrangian–Eulerian method (see Table 1). The pros and cons of these numerical models have been discussed in detail in a recent review paper by Wörner (2012). Recently, phase-field model based on Cahn–Hilliard equation has been successfully applied to the simulations of various multiphase flow problems, including the wetting phenomenon of droplets (Takada and Tomiyama 2007; Liu and Zhang 2010), electro-hydrodynamics (Lin et al. 2012), flow in micro-channels (Wylock et al. 2012) and viscoelasticity (Zhou et al. 2010). One of the advantages of the phase-field method is that it naturally allows the contact line of a droplet to move along the wetted surface without any ad hoc treatment for stress singularity (see Sect. 2.2). Therefore, the model is favorable for simulations involving contact-line motion on a wetted surface. However, since phase-field model involves fourth-order derivative (see Eqs. 4, 5), numerical computation is more complex and time consuming. Hence, a simple boundary condition which is desirable for computational efficiency has been proposed in this study for the modeling of dynamic contact angle (Sect. 3.2).

2.1 Governing equations

Detailed theoretical development of the phase-field model and its application for fluid flow simulation as described here can be found in the literature (Yue et al. 2004; Jacqmin 1999, 2000). Only the basic concept of the model and governing equations employed for the current simulation are highlighted here. A phase-field model describes a system of two phases which are separated by a diffuse interface of finite thickness. The profile and thickness of the interface are determined by the molecular attraction and random molecular motion. The evolution of the interfacial layer is governed by a phase-field function ϕ through the Cahn–Hilliard equation (Yue et al. 2004),

$$\frac{\partial \phi}{\mathrm{d}t} + \mathbf{u} \cdot \nabla \phi = \nabla \cdot (\kappa \nabla G) \tag{1}$$

where $\mathbf{u}$ = velocity field, κ = phase-field mobility and G = chemical potential. The concentrations or volume fractions of phase 1 and phase 2 are $(1 - \phi)/2$ and $(1 + \phi)/2$, respectively. ϕ assumes the value of -1 and $+1$ in the regions with only phase 1 and phase 2, respectively. At the thin interfacial region between the two fluids, ϕ varies sharply but continuously from -1 to $+1$.

The second term on the left-hand side of Eq. 1 governs the changes in ϕ through convective effect. The term on the right-hand side of Eq. 1 represents the diffusive effect due to the gradient of chemical potential G.

Table 1 Recent numerical simulations of droplet spreading and impingement on solid surface

Researchers	Type of surface	Initial condition of droplet	Weber number	Simulation method
Ganesan (2013)	Homogeneous	Impinging droplet	34–798	Arbitrary Lagrangian–Eulerian with finite element
Lee and Liu (2010)	Homogeneous	Impinging droplet	13 and 108	Lattice Boltzmann
Mukherjee and Abraham (2007)	Homogeneous	Impinging droplet	27–756	Lattice Boltzmann
Kwak et al. (2011)	Homogeneous	Impinging droplet	1.63	Level set
Yokoi et al. (2009)	Homogeneous	Impinging droplet	31.7	Coupled volume of fluid and level set
Sato and Niceno (2012)	Homogenous	Semi-spherical sessile droplet	0	Conservative level set
Seveno et al. (2011)	Homogenous	Spherical droplet in contact with surface	0	Molecular dynamics
Briones et al. (2010)	Homogeneous	Impinging droplet	1.4–35.3	Volume of fluid
Roisman et al. (2008)	Homogeneous	Impinging droplet	0.88–1.81	Volume of fluid
Fujimoto et al. (2007)	Homogeneous and inclined surface	Impinging droplet	56	Volume of fluid
Lunkad et al. (2007)	Homogeneous and inclined surface	Impinging droplet	51–391	Volume of fluid
Zhou et al. (2010)	Homogeneous	Semi-spherical and elongated sessile droplet	0	Phase field
Kusumaatmaja and Yeomans (2007)	Chemically patterned and superhydrophobic	Semi-spherical sessile droplet, with increasing volume	0	Lattice Boltzmann
Yan and Zu (2007)	Heterogeneous wettability	Spherical droplet in contact with surface	0	Lattice Boltzmann
Kusumaatmaja et al. (2008)	Micro-parallel grooves	Semi-spherical sessile droplet	0	Lattice Boltzmann
Takada and Tomiyama (2007)	Heterogeneous wettability	Semi-spherical sessile droplet	0	Phase field
Xu and Qian (2012)	Wettability gradient	Two dimensional semi-circular sessile droplet	0	Phase field

$$G = \lambda_m \left[-\nabla^2 \phi + \frac{\phi(\phi^2 - 1)}{\varepsilon^2} \right] \qquad (2)$$

where λ_m = mixing energy density and ε = interfacial thickness. The first term on the right-hand side of Eq. 2 represents the interfacial energy, while the second term represents the bulk free energy.

Phase-field mobility κ determines the timescale of Cahn–Hilliard diffusion and relaxation time of the interface. κ should be chosen to be large enough to retain a constant interfacial thickness but small enough so that the convective term is not overdamped. The mixing energy density is related to the surface tension σ through the expression (Yue et al. 2004)

$$\sigma = \frac{2\sqrt{2}}{3} \frac{\lambda_m}{\varepsilon} \qquad (3)$$

To facilitate the solving process, Eq. 1 which is a fourth-order partial differential equation (PDE) is separated into two second-order PDEs as follows:

$$\frac{\partial \phi}{\mathrm{d}t} + \mathbf{u} \cdot \nabla \phi = \frac{\kappa \lambda_m}{\varepsilon^2} \nabla^2 \psi \qquad (4)$$

$$\psi = -\varepsilon^2 \nabla^2 \phi + \phi(\phi^2 - 1) \qquad (5)$$

Fluid flow is modeled with the Navier–Stokes equation and continuity equation:

$$\rho \left(\frac{\mathrm{d}\mathbf{u}}{\mathrm{d}t} + \mathbf{u} \cdot \nabla \mathbf{u} \right) = -\nabla p + \mu \nabla^2 \mathbf{u} + \rho \mathbf{g} + G \nabla \phi \qquad (6)$$

$$\nabla \cdot \mathbf{u} = 0 \qquad (7)$$

where p = pressure and $\mathbf{g}$ = gravitational acceleration. The density and dynamic viscosity are written with respect to the volume fraction of fluid 2 V_f as

$$\rho = \rho_1 + (\rho_2 - \rho_1)V_f, \quad \mu = \mu_1 + (\mu_2 - \mu_1)V_f; \\ V_f = (1 + \phi)/2 \qquad (8)$$

where ρ_1 and ρ_2 are the densities of phase 1 and phase 2, respectively, and μ_1 and μ_2 are the dynamic viscosities of phase 1 and phase 2, respectively. Hence, the properties of

the fluids/phases vary continuously with phase-field function across the thin interfacial region. The last term of Eq. 6 represents the surface tension force. Although it is implemented as a body force, the surface tension force only has a finite value at the interfacial region where the gradient of ϕ is nonzero.

The governing equations (Eqs. 1, 6 and 7) are non-dimensionalized based on characteristic length D (diameter of droplet before impact), impact velocity U ($\mathbf{u} = U\,\mathbf{u}^*$), gravitation acceleration g ($\mathbf{g} = g\,\mathbf{g}^*$), time ($t = t^*D/U$) and pressure ($p = p^*\rho U^2$):

$$\frac{\partial \phi}{\mathrm{d}t^*} + \mathbf{u}^* \cdot \nabla \phi = \frac{3}{2\sqrt{2}}\frac{1}{Pe}\nabla^2\left[-Cn^2\nabla^2\phi + \phi(\phi^2 - 1)\right]$$

(9)

$$\left(\frac{\mathrm{d}\mathbf{u}^*}{\mathrm{d}t^*} + \mathbf{u}^* \cdot \nabla \mathbf{u}^*\right) = -\nabla p^* + \frac{1}{Re}\nabla^2\mathbf{u}^* + \frac{1}{Fr}\mathbf{g}^*$$
$$+ \frac{3}{2\sqrt{2}}\frac{1}{Cn \cdot We}\left[-Cn^2\nabla^2\phi + \phi(\phi^2 - 1)\right]\nabla\phi$$

(10)

$$\nabla \cdot \mathbf{u}^* = 0$$

(11)

From the dimensionless governing equations, the following dimensionless numbers can be identified:

$$Pe = \frac{DU\varepsilon}{\kappa\gamma}, \quad Cn = \frac{\varepsilon}{D}, \quad Re = \frac{\rho UD}{\mu}, \quad Fr = \frac{U^2}{gD},$$
$$We = \frac{\rho U^2 D}{\sigma}.$$

(12)

Peclet number Pe defines the ratio of convective to diffusive mass transport of the two-phase system. Cahn number Cn shows the relative thickness of the interfacial layer with respect to the diameter of the droplet. Reynolds number Re describes the ratio of inertial force to viscous force, while Weber number We shows the ratio between inertial force to surface tension force. Froude number Fr defines the ratio of the velocity of the droplet to the gravitational acceleration. In our studies, U ranges from 0.5 to 4 m s^{-1} (see Sect. 3.4.3) and ε is set to 1 μm (see Sect. 3.1). Based on the liquid properties shown in Table 2, these dimensionless parameters are calculated to be $Pe = 3.4$–27, $Cn = 0.018$, $Re = 31$–247, $We = 0.18$–12 and $Fr = 463$–$29{,}654$.

The simulation is divided into three parts. In the first part, the simulation of a droplet impinging and spreading on a homogeneous surface was conducted. The simulation result was compared with experimental results available in the literature to validate the model. It also serves as a benchmark and as a special case for the second part of the simulation. The second part of the simulation investigated droplet impinging and spreading on a circular area with a lower contact angle (higher wettability) than the surrounding surface. Water droplet tends to wet a surface with

Table 2 Symbols and constants in numerical simulation

Constant	Symbol (unit)	Value
Phase-field mobility	κ (m^3 skg^{-1})	1.10×10^{-10}
Liquid–air surface tension	σ (N m^{-1})	0.0728
Density of air	ρ_1 (kg m^{-3})	1.2
Density of water	ρ_2 (kg m^{-3})	1,000
Viscosity of air	μ_1 (Pa s)	2×10^{-5}
Viscosity of water	μ_2 (Pa s)	8.9×10^{-4}
Molecular displacement length	λ (m)	2×10^{-10}
Boltzmann constant	k_b (m^2 kg s^{-2} K^{-1})	1.381×10^{-23}
Temperature	T (K)	293
Droplet initial diameter	D (m)	5.5×10^{-5}

lower contact angle (higher surface energy) instead of a surface with higher contact angle (lower surface energy) to lower the overall energy of the system. Therefore, on a circular area with a lower contact angle than the surrounding surface, the droplet is expected to be contained and conformed to the circular pattern. In the third part, a droplet impinging on a long rectangular stripe pattern with a lower contact angle as compared to the surrounding surface was presented. In this study, evaporation effect can be neglected in the simulation of droplet impingement due to the 4 order of magnitude difference in their characteristic timescale (Briones et al. 2010). The surface is also assumed to be smooth, and the change in wettability is due to chemical heterogeneity alone. The droplet and surface are also assumed to be isothermal. No splashing of droplet is expected since We is lower than 100 (Mani et al. 2010) in all our simulations.

2.2 Boundary conditions

The numerical model was implemented with the finite element method (FEM) software, COMSOL Multiphysics. The first two parts of the simulations are axisymmetrical, and the simulation domain is shown in Fig. 1. When a droplet partially wets a solid surface, typical contact-line models which assume a moving sharp interface separating the two phases (with no flux through the interface) would induce a singularity at the contact line upon the imposition of no-slip boundary condition. However, under the phase-field model which assumes a diffusive interface, no-slip boundary condition can be applied without any complication at the contact line (Seppecher 1996). The interface in a phase-field model can move across the wetted surface with a diffusive effect instead of just the convective effect while maintaining the interface form and stability (Jacqmin 2000).
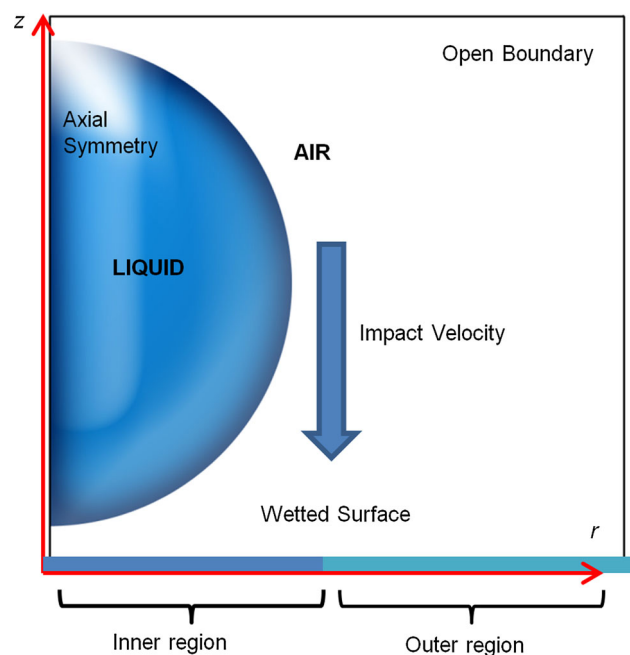
Fig. 1 Computation domain for axisymmetry simulation

The contact angle boundary condition at the wetted surface is specified according to the following equation:

$$\cos \theta_a = \frac{\mathbf{n} \cdot \nabla \phi}{|\nabla \phi|} \qquad (13)$$

where θ_a = apparent contact angle and $\mathbf{n}$ = normal vector into the wetted surface. In the first part of the simulation, three different types of boundary conditions related to the definition of apparent contact angle are examined. The simplest condition is to set the apparent contact angle to be the static contact angle (SCA) θ_s of the droplet, with the assumption that the apparent contact angle is constant throughout the wetting process. In general, the dynamic contact angle (DCA) at the moving contact line differs from its static value and changes throughout the spreading process. Specifically, the advancing DCA is greater than the SCA, while the receding DCA is smaller than the SCA. There are two major approaches to describe these changes of apparent contact angle with respect to the velocity of contact line, namely hydrodynamic approach (Cox 1986; Voinov 1976) and molecular–kinetic approach (Blake and De Coninck 2002).

According to hydrodynamics theory, the change of dynamic contact angle is caused by viscous bending of liquid–gas interface on a mesoscopic scale. In its simplest form, it can be expressed (Voinov 1976) by

$$\theta_a^3 - \theta_m^3 = 9\mathrm{Ca_s} \ln\left(\frac{L}{L_m}\right), \qquad \theta_a < \frac{3}{4}\pi \qquad (14)$$

where $\mathrm{Ca_s}$ = spreading capillary number and θ_m = microscopic contact angle which is often assumed to be the static contact angle θ_s. L and L_m are the macroscopic and microscopic characteristic lengths, respectively, and are often regarded as fitting parameters in most analyses. Here, the spreading capillary number is defined as $\mu v_{cl}/\sigma$ where v_{cl} = contact-line velocity. Typically, L is set to 10 μm, which is the approximate distance from the wetting line where the contact angle can be measured, and L_m = 1 nm which is of the order of molecular size, and thus, $\ln(L/L_m)$ = 9.21 (Blake 2006; Cox 1986). Typical values of $\ln(L/L_m)$ derived from curve fitting of experimental results are found to be around 10 (Seveno et al. 2009).

An alternative approach to model the change in dynamic contact angle is through a molecular kinetic approach. According to the molecular kinetic theory, the movement of the contact line is due to the displacement of molecules in one phase on the solid surface adsorption site by molecules from another phase. The out-of-balance surface tension, which is defined as $\sigma(\cos\theta_a - \cos\theta_s)$, provides the energy for this molecular displacement process. It accounts for the deviation of dynamic contact angle from its static value (Blake and De Coninck 2002). The contact-line velocity v_{cl} can be expressed as

$$v_{cl} = 2f_o\lambda \sinh\left[\frac{\sigma\lambda^2}{2k_bT}(\cos\theta_s - \cos\theta_a)\right] \qquad (15)$$

where f_o = characteristic frequency of molecular displacement, λ = molecular displacement length, k_b = Boltzmann constant and T = temperature. f_o is defined as

$$f_o = \frac{hf_o^s}{v_m\mu} \qquad (16)$$

where h = Planck constant, f_o^s = equilibrium frequency of molecular displacement when retarded only by solid–liquid interaction and v_m = molecular flow volume. For this study, the simulation results will be compared with the experimental results obtained by Briones et al. (2010), with λ taken to be 0.2 nm following their analysis. Other simulation parameters and constants are shown in Table 2. Phase 1 refers to air, while phase 2 refers to water in this study.

As suggested by de Gennes (1985), for a partially wetting droplet, the out-of-balance surface tension which causes the deviation of dynamic contact angle from its static value can be compensated by 2 distinct channels of dissipation: dissipation in the bulk and in the microscopic region near the contact line. These two modes of dissipation correspond to the two types of DCA boundary conditions described here. Hydrodynamic model would better describe the situation where bulk viscous dissipation is dominant. Molecular–kinetic model would be more suitable if the dominant mode of dissipation is due to adsorption/desorption of fluid molecules on the solid surface near the contact line. More complicated models which

incorporate both these dissipation channels will not be discussed here.

3 Results and discussions

3.1 Convergence of phase-field simulation

In a real physical system, the two-phase interface width is much smaller (in the order of a few angstroms) and sharper than the characteristic diffusive interface thickness ε adopted in most phase-field simulations. However, a numerical simulation with such fine interface width is not feasible due to limited computation resources as mesh size will have to be adjusted to the order of ε for accurate resolution of the phase-field function at the interface. Therefore, a phase-field simulation is only valid if the simulation result is not affected significantly by the change in interface width, i.e., the simulation produces result which converges according to a sharp-interface model.

Yue et al. (2010) proposed a criterion for the sharp-interface limit in the situation where a fluid interface contacts a solid wall:

$$Cn \leq \frac{4\sqrt{\kappa\mu_e}}{D}, \quad \mu_e = \sqrt{\mu_1\mu_2} \qquad (17)$$

where μ_e is the equivalent viscosity for the two fluids.

The first set of simulations will be conducted based on SCA boundary condition with three different mesh sizes for a convergence test. The value of interfacial thickness ε is typically set to half of the mesh size employed in the simulation. Smaller mesh size and ε provide better resolution to capture the sharp change in phase-field function ϕ across the fluid–air interface. The minimum value of ε is set to 0.5 μm for the convergence test because smaller ε and finer mesh require excessive computation time and memory. For a converged solution of a moving contact line problem, κ should be independent on ε (Yue et al. 2010). Based on the smallest mesh size which allows a solution to be obtained with our computational resources, the minimum κ is calculated to be 1.10×10^{-10} m^3 s kg^{-1} (from Eq. 17), and this value is adopted for three different mesh sizes. The impact velocity is set to 2.45 m s^{-1}, and the SCA θ_s is set to 55° to compare with experimental results obtained from the literature [droplet C in Briones et al. (2010)]. The simulated time evolution of droplet spreading diameter for three values of ε (0.5, 1.0 and 2.0 μm, which correspond to $Cn = 0.009$, 0.018 and 0.036, respectively) is shown in Fig. 2. The spreading diameter of the droplet on the wetted surface can be obtained by integrating the volume fraction of fluid 2 (droplet), V_f along the wetted surface. The dimensionless spread diameter $D*$ is defined as

$$D*(t) = \frac{2\int V_f(t)dr}{D} \qquad (18)$$

Based on the definition of V_f, $V_f = 1$ at the surface wetted by the droplet and $V_f = 0$ at the surface outside of the droplet. V_f varies gradually from 1 to 0 at the interfacial region between liquid and air. The integrand in Eq. 18 is zero outside of the droplet, where $V_f = 0$. Thus, the
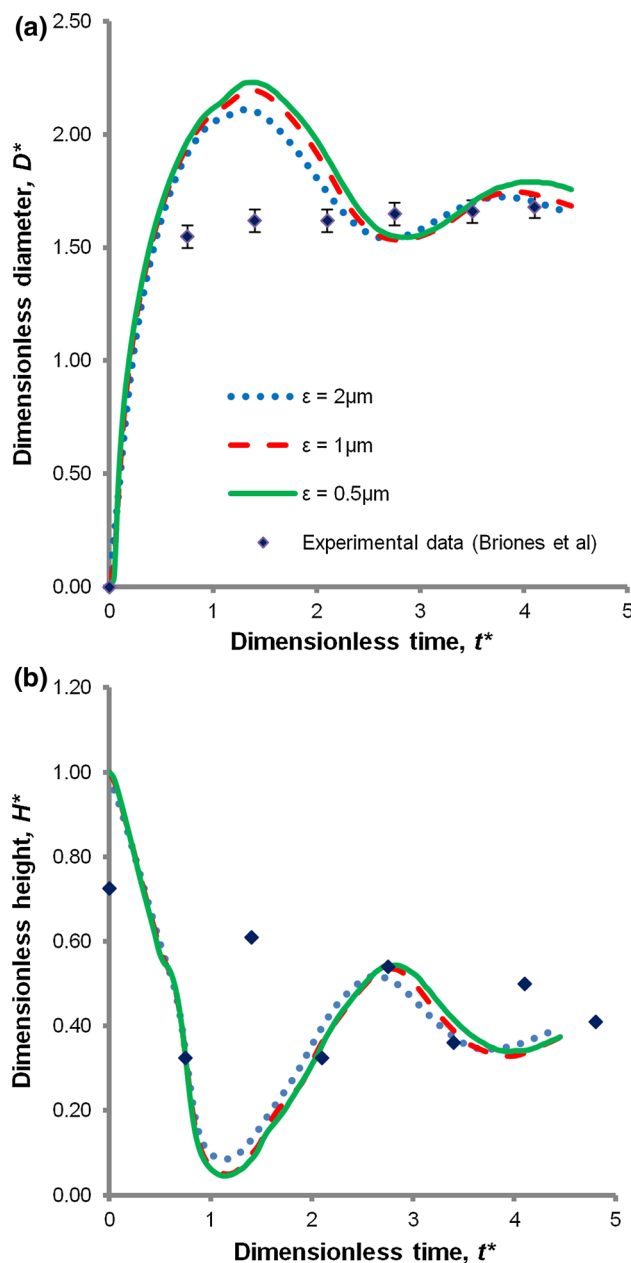

Fig. 2 Comparisons between phase-field simulation based on SCA boundary condition with different interfacial thickness ε and experimental results (Briones et al. 2010). Both **a** droplet spread diameter $D*$ and **b** height $H*$ are non-dimensionalized with droplet initial diameter ($D = 55$ μm). Impact velocity, $U = 2.45$ m s^{-1}; static contact angle $\theta_s = 55°$; $We = 4.5$. Dimensionless time $t* = tU/D$

integration operation in Eq. 18 yields the equivalent radius of the droplet. Similarly, the height of the droplet $H*$ can be obtained by integrating V_f along the symmetry axis and non-dimensionalized with D. It is noted that the spreading diameter and droplet height for $\varepsilon = 0.5$ μm and $\varepsilon = 1.0$ μm do not differ significantly (see Fig. 2), indicating convergence has been achieved. The intermediate value $\varepsilon = 1.0$ μm is chosen for subsequent analysis because a relatively accurate solution can be obtained in an acceptable time frame.

To determine the stability of the phase-field function during spreading, the average gradient of phase-field function at the middle of the interfacial region (where the curve is approximately linear, see Fig. 3) on the wetted surface was determined from the numerical results for the three interfacial thicknesses throughout the wetting process. As expected, the average gradients of ϕ are dependent on the interface thickness and were determined to be 2.31×10^5 m^{-1} (standard deviation 0.078×10^5), 4.73×10^5 m^{-1} (standard deviation 0.123×10^5) and 9.69×10^5 m^{-1} (standard deviation 0.235×10^5) for ε values of 2, 1 and 0.5 μm, respectively. The phase-field function gradient at the interfacial region can be approximated as a constant, especially for $\varepsilon = 0.5$ μm and $\varepsilon = 1$ μm, where the standard deviations are less than 2.6 %. The solution is less accurate when ε is set to a large value due to the excessively diffused interfacial region. A simple scheme based on the interfacial gradient of phase-field function has been formulated to track the contact-line velocity for the specification of DCA boundary condition, as described in Sect. 3.2.

3.2 Tracking of contact-line velocity

The two models of DCA described in Sect. 2.2 require the specification of contact-line velocity at the wetted boundary/wall. Unlike other models which specify at the contact surface a slip velocity which can be prescribed in terms of the local fluid velocity, the phase-field model adopted in this study specifies a non-slip boundary condition at the wall. Hence, the fluid velocity at the wall is zero, and the contact-line velocity cannot be prescribed with respect to the local fluid velocity. A simple scheme for the tracking of contact-line velocity is proposed based on the phase-field function gradient in the interfacial region (see Fig. 3).

If the phase-field function gradient $d\phi/dr$ is known, the velocity of the moving contact line can be written as a function of the local time derivative of phase-field function $d\phi/dt$, as follows:

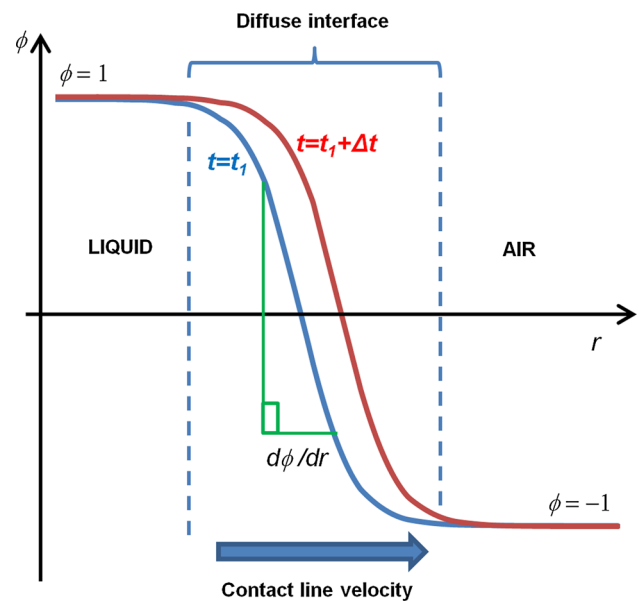$$v_{cl}(t) = -\frac{d\phi/dt}{d\phi/dr} \qquad (19)$$

Fig. 3 Contact-line velocity tracking scheme is illustrated with schematic showing spatial distribution of phase-field function ϕ at two time steps (t_1 and $t_1 + \Delta t$). If phase-field function gradient $d\phi/dr$ is constant with time, contact-line velocity can be written as $v_{cl} = -(d\phi/dt)/(d\phi/dr)$

If $d\phi/dr$ is assumed to be a constant during the spreading process, the contact-line velocity will assume a finite value at the interfacial region according to the time variation of ϕ; ϕ outside of the interfacial region (in the region with only air or liquid) is constant with time. When the contact line is advancing, ϕ at the interfacial region increases with time; when the contact line is receding, ϕ at the interfacial region decreases with time.

To determine whether the phase-field function gradient changes with surface wettability, a series of simulations for droplet spreading on surfaces of different contact angles was performed and the average interfacial phase-field gradient for each simulation was measured. Figure 4 shows that the interfacial phase-field gradient varies weakly with SCA of a surface, and a quadratic curve can be fitted through the points. In the simulation of droplet spreading on a surface with heterogeneous wettability, the interfacial phase-field gradient can be associated with the local SCA of the surface.

Although the spatial gradient of the phase-field function is constant during the spreading process, it is noted that the gradient does change for a short period of time, just when the droplet impinges on the surface. This transient behavior of the phase-field gradient during the impact process is not included in the boundary condition specification for this simplified model and will be investigated in future work.
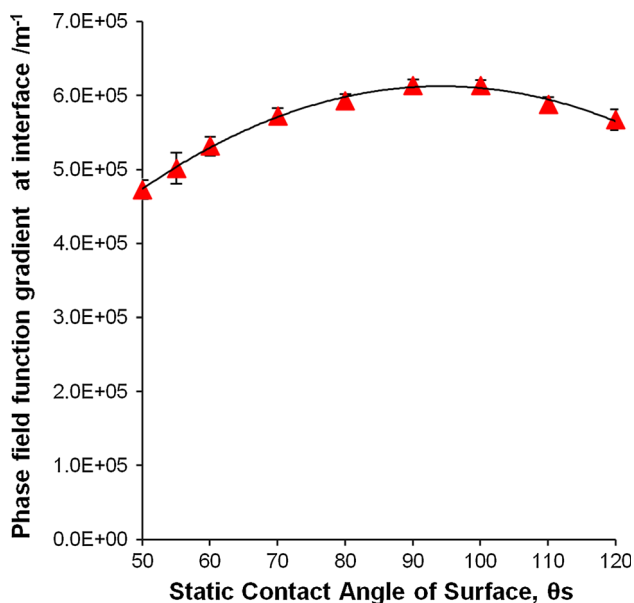
Fig. 4 Average gradient of phase-field function at fluid–air interface on surfaces with different contact angles

3.3 Validation of phase-field model with experimental results

To verify the validity of the phase-field model and to determine the phenomenological constants for DCA boundary conditions, the numerical results were compared with experimental results obtained from the literature [droplet C in Briones et al. (2010)]. Figure 2 shows that the numerical results of the spreading diameter obtained from SCA boundary conditions as compared to the experimentally obtained spread diameter under the same conditions. The equilibrium droplet diameter predicted by the SCA model fits the experimental results very well. However, the numerical results show a high overshoot in spreading diameter upon impact and the predicted maximum spread diameter is 35 % larger than the spread diameter observed experimentally. Thus, SCA model cannot predict the droplet spreading dynamics upon impact accurately. Lunkad et al. (2007) reported that droplet spreading dynamics on a horizontal surface can only be modeled accurately with SCA model if the surface is less wettable (contact angle >90°). Therefore, DCA models, namely the hydrodynamic model and molecular–kinetic model, are considered in this study.

Three simulations based on the hydrodynamics approach for DCA boundary condition were conducted by taking values of $\ln(L/L_m)$ as 9.2, 18 and 72 (see Fig. 5). As mentioned in Sect. 2.2, physically realistic values of $\ln(L/L_m)$ should be around 10. However, a good fit of the hydrodynamic model on experimental spreading diameter (see Fig. 5) can only be obtained at $\ln(L/L_m) = 72$, which would result in subatomic value for the microscopic length
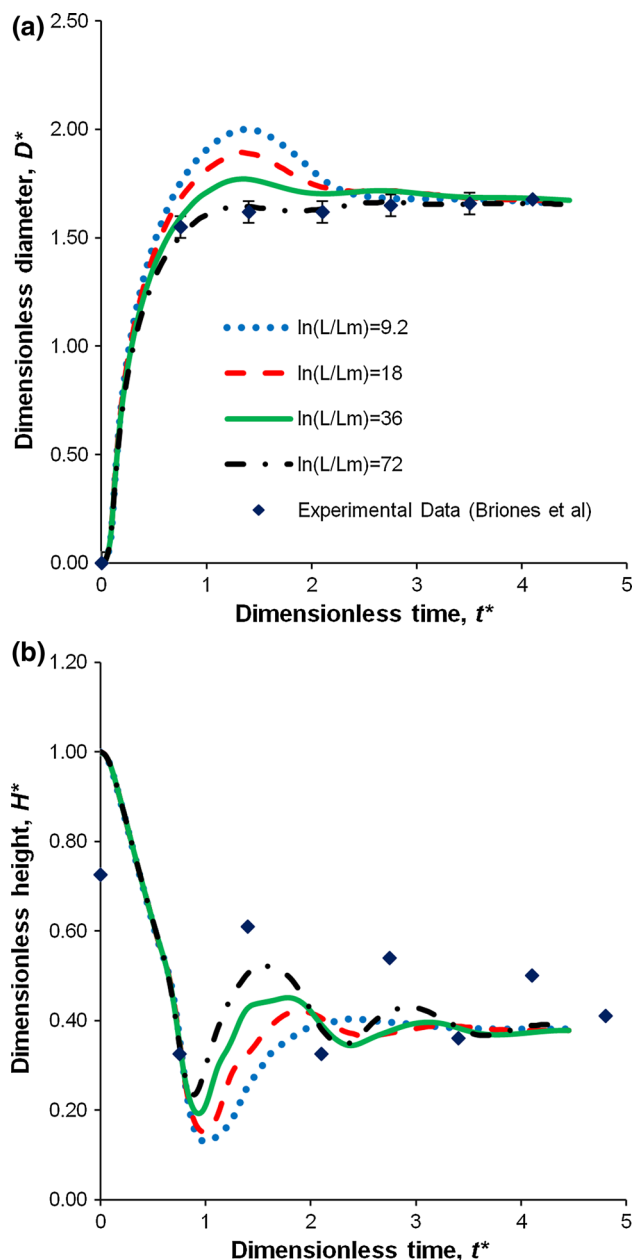

Fig. 5 Comparisons between phase-field simulation based on DCA boundary condition formulated with hydrodynamic theory and experimental results (Briones et al. 2010). Both **a** droplet spread diameter D^* and **b** height H^* are non-dimensionalized with droplet initial diameter ($D = 55$ μm). Impact velocity $U = 2.45$ m s^{-1}; static contact angle $\theta_s = 55°$; $We = 4.5$; dimensionless time $t^* = tU/D$; $L =$ macroscopic characteristic length scale, $L_m =$ microscopic characteristic length scale

scale L_m. This indicates that viscous effect may not be the main mode of energy dissipation during the wetting process. For high contact-line velocity and larger contact angle, energy dissipation at the contact line due to molecular kinetics is dominant. In contrast, for lower contact angle with the displaced fluid of higher viscosity than the displacing fluid, energy dissipation is better

described by hydrodynamic theory (Brochard-Wyart and de Gennes 1992). Hence, for our study here which involves high impact velocities, molecular–kinetic theory was employed for the specification of DCA boundary condition.

Three simulations based on molecular–kinetic approach for DCA boundary condition were conducted by assuming the characteristic frequency of molecular displacement $f_o = 10$, 20 or 40 GHz (see Fig. 6). A good fit to the experimental results can be obtained with $f_o = 10$ GHz, which has the same order of magnitude as most f_o values employed in the literature (Seveno et al. 2004; Blake et al. 1997; Briones et al. 2010; Bhardwaj and Attinger 2008). The main mode of energy dissipation near the contact line can be attributed to the adsorption/desorption of fluid molecule on the solid surface in this case. Despite the accuracy in the prediction of spread diameter, the height of the droplet seems to be overdamped in the numerical simulation (see Fig. 6b), which is also reported by Briones et al. (2010). Molecular–kinetic approach (Blake's formulation, Eq. 15) is adopted for subsequent simulation in Sect. 3.4 since it produces results which are closest to the experimental data.

3.4 Impact and spreading on circular pattern with wettability contrast

In this section, simulation results of a droplet impinging and spreading on a surface with a circular heterogeneous pattern are presented. All numerical results in Sect. 3.4 were obtained through the molecular–kinetic boundary condition on wetted surface (Eq. 15). The inner region of the circular pattern is more wettable than the surface surrounding it. The contact angle transition on the wetted surface was modeled with a smoothed Heaviside function. The effect of wettability contrast, circular pattern diameter and impact velocity were investigated and discussed in Sects. 3.4.1–3.4.3.

3.4.1 Effect of wettability contrast

In this series of simulations, the contact angle of the inner surface (see Fig. 1) is fixed at 50°, while the contact angle of the outer region is set to 4 different values ranging from 50° to 120°. The water contact angle on a surface is dependent on the property of the material. Some examples of contact angles for common substrates are poly(ethylene terephthalate) PET with SCA = 82° (Blake 2012), poly(methyl methacrylate) PMMA with SCA = 77° (Wang et al. 2011), polystyrene (PS) with SCA = 93° (Jung and Bhushan 2006) and silicon wafer with SCA = 51° (Tao and Bhushan 2006). The contact angles of these common substrates fall within the range of SCA simulated (50°–120°) and thus represent realistic
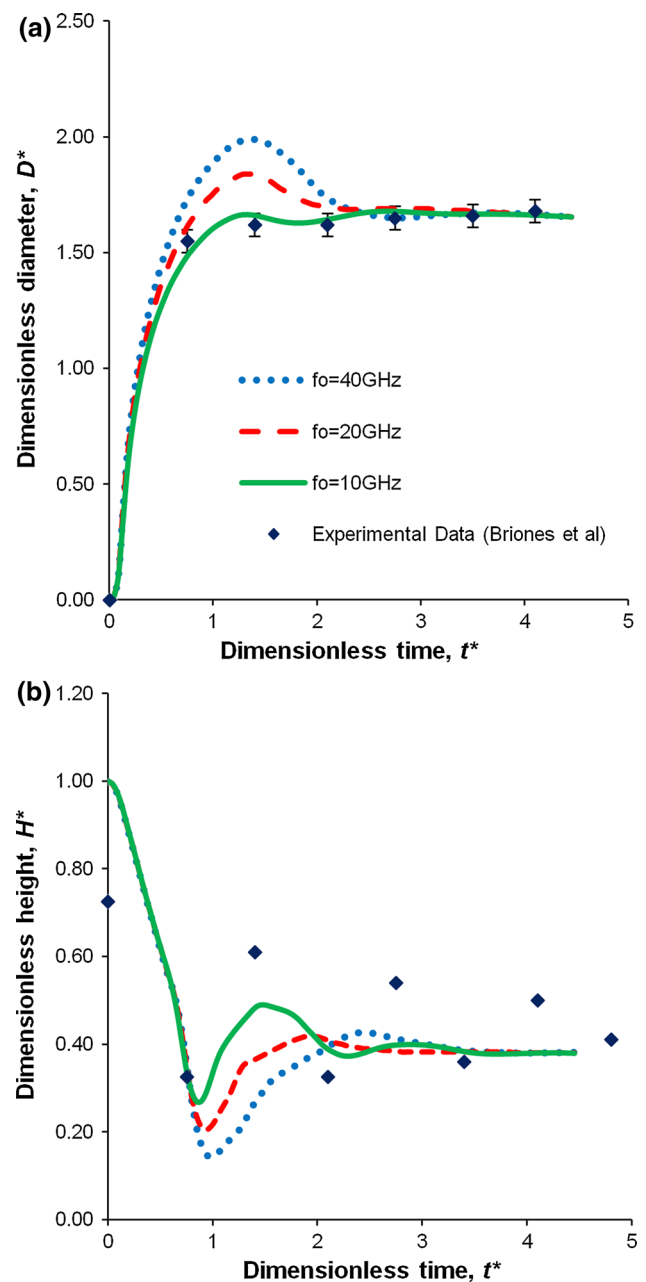

Fig. 6 Comparisons between phase-field simulation based on DCA boundary condition formulated with molecular–kinetic theory and experimental results (Briones et al. 2010). Both **a** droplet spread diameter D^* and **b** height H^* are non-dimensionalized with droplet initial diameter (55 μm). Impact velocity $U = 2.45$ m s^{-1}; static contact angle $\theta_s = 55°$; $We = 4.5$; dimensionless time $t^* = tU/D$; f_o = characteristic frequency of molecular displacement

properties of the surface. In addition, it should be noted that the contact angle or surface properties of a substrate can be modified selectively with methods such as chemical coating (Jung and Bhushan 2006), femto-second laser irradiation (Wang et al. 2011) or plasma treatment (Lai et al. 2006).

The diameter of the droplet and the impact velocity are set to 55 μm and 2.45 m s^{-1}, respectively. The typical droplet diameter produced by an inkjet dispenser ranges from 10 to 100 μm (Hutchings and Martin 2013). The simulated droplet diameter of 55 μm is the average of the range. The diameter of the circular pattern D_h is set to 70 μm (non-dimensionalized with the initial droplet diameter; $D_h* = 1.27$), which is smaller than the final droplet spread diameter on a homogeneous surface (1.65D). Figure 7 shows the comparison between the simulated droplet impinging on a homogeneous surface and a circular region with 70° wettability contrast. On the surface with 70° wettability contrast, the droplet is confined in the circular region with a diameter of 70 μm which is smaller than the droplet's final diameter on a homogeneous surface (91 μm).

The time evolution of spreading diameter for two surfaces (the surface inside and outside of the circular pattern) with various wettability contrast is shown in Fig. 8a. The simulation results show that even a slight wettability contrast (such as 5°) produces a notable reduction in final spreading diameter. The final spread diameter reduces gradually with increasing wettability contrast and approaches an asymptotic limit beyond 70° difference (see Fig. 8b).

In addition to the final spread diameter, the maximum spread diameter was also inspected. Similar to the final droplet diameter, the maximum diameter reduces with increasing wettability contrast (see Fig. 8b). Percentage overshoot is defined as (maximum spread diameter/final spread diameter − 1) × 100 %. For a homogeneous surface (0°) or a surface with small (5°) wettability contrast, the droplet reaches the final spread diameter without a significant overshoot (see Fig. 8b). However, with higher wettability contrast (20° and 40°), the spreading diameter shows a significant overshoot of 9–10 % before receding to the final diameter. For the surface with very large wettability contrast (70°), the droplet exhibits a smaller overshoot (4 %) in spread diameter and conforms to the circular pattern. This illustrates that chemical surface patterning with a pattern of high wettability contrast is a viable technique to constrain the spreading of an impinging droplet to a specified area. In some applications where the deposited droplets are in close proximity to each other, sufficiently high wettability contrast is required to ensure that the droplet does not spread beyond the confined area and interfere with the adjacent droplets.

Ren and E (2011) investigated the effect of surface wettability contrast on the movement of contact line over a surface with sinusoidal contact angle (see Fig. 9a). Their analysis is adapted here for the current investigation of a droplet spreading over a surface with a step change of wettability (see Fig. 9b). If the argument of hyperbolic sine in Eq. 15 is small, the DCA boundary condition based on Eq. 15 can be approximated as (Ren and E 2011)
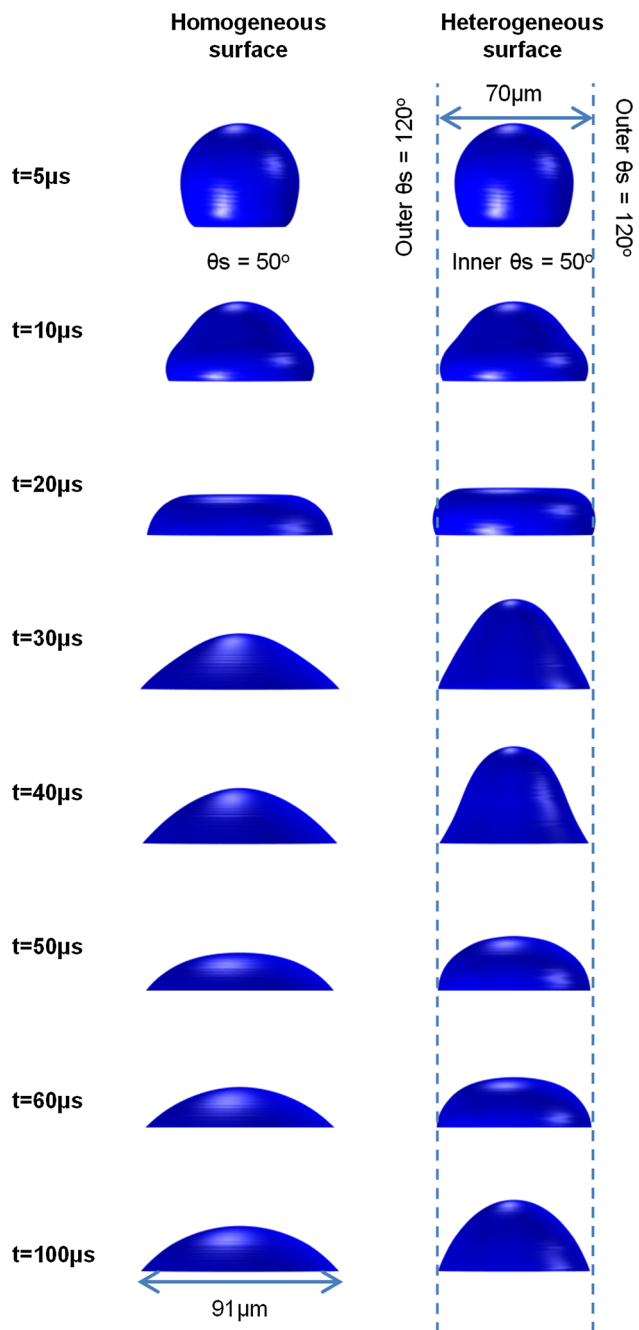

Fig. 7 Comparisons between simulated droplet impinging on a homogeneous surface with static contact angle = 50° and a circular area with 70° wettability contrast to surrounding surface. Droplet initial diameter $D = 55$ μm; impact velocity $U = 2.45$ m s^{-1}; $We = 4.5$

$$v_{cl} = \frac{f_o \sigma \lambda^3}{k_b T} \cos(\theta_s - \cos \theta_a) \tag{20}$$

Equation 20 can be rewritten as:

$$\sigma \cos(\theta_s - \cos \theta_a) = \beta v_{cl}, \quad \beta = \frac{k_b T}{f_o \lambda^3} \tag{21}$$
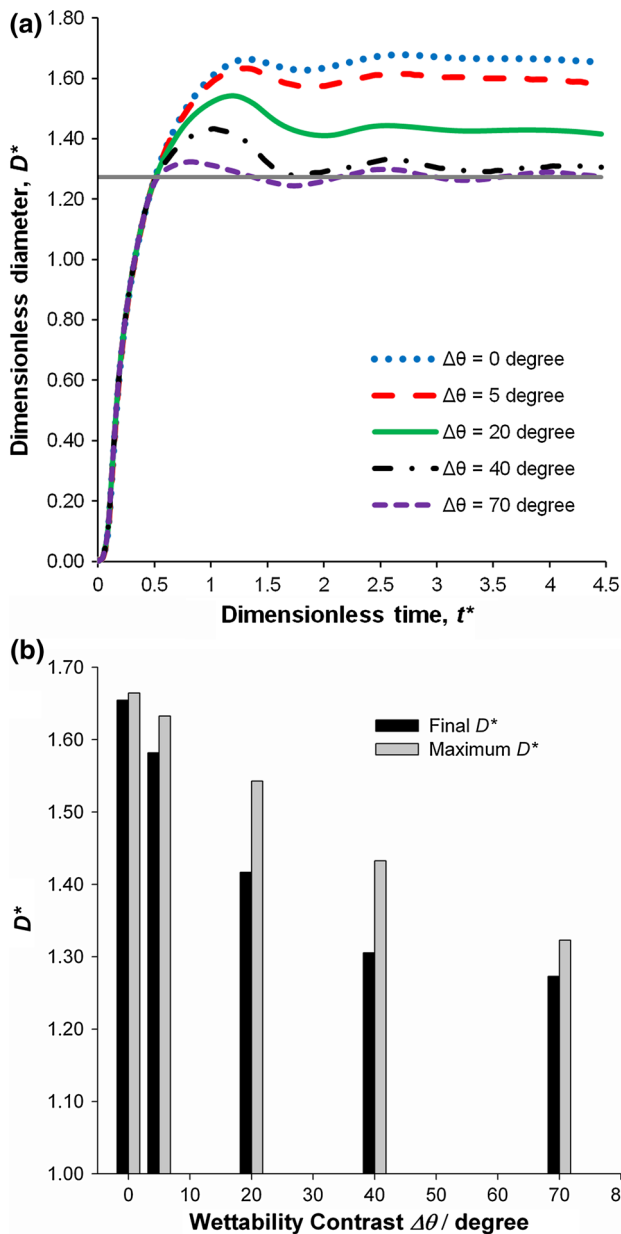
(a)

(b)

Fig. 8 **a** Time evolution of droplet spread diameter (non-dimensionalized with droplet initial diameter) upon impingement on a circular pattern with various wettability contrasts $\Delta\theta$ to surrounding surface. *Horizontal line* at $D_h^* = 1.27$ indicates diameter of circular pattern. **b** Final droplet spread diameter and maximum spread diameter (non-dimensionalized with droplet initial diameter) for droplet impinging on a circular pattern with various wettability contrast $\Delta\theta$ to surrounding surface. Droplet initial diameter $D = 55$ μm; impact velocity $U = 2.45$ m s^{-1}; $We = 4.5$; dimensionless time $t^* = tU/D$

where β = friction parameter, which describes the three-phase interaction at the contact line (Ren et al. 2010). Although Eq. 20 is only valid if the apparent contact angle is close to the static contact angle, this simplified analysis provides meaningful insight to gain an understanding of the numerical simulation results.
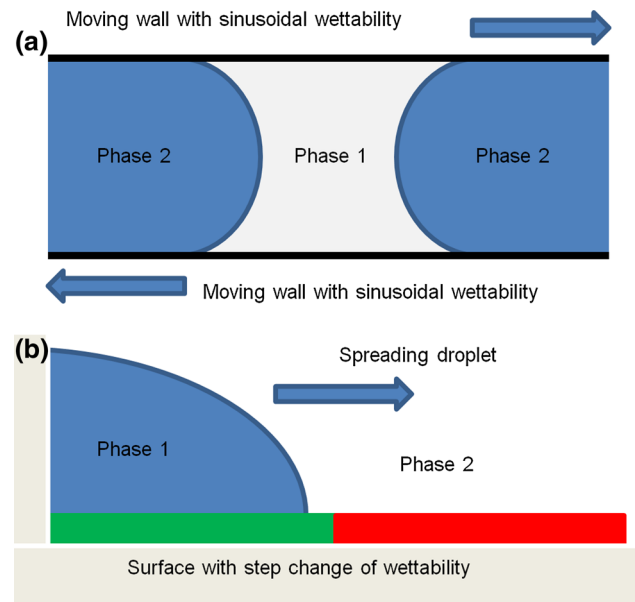
Fig. 9 **a** Schematic of theoretical analysis by Ren and E (2011) on movement of contact line over surface with sinusoidal wettability. **b** Analysis performed in this study on spreading droplet across surface with step change of wettability

For a droplet spreading on a heterogeneous surface, the following relationship can be established based on Young's equation (Ren and E 2011):

$$\sigma \cos\theta_s(r) = \gamma_2(r) - \gamma_1(r) \tag{22}$$

$$\sigma \cos\theta_s(r) = \Delta\sigma_o + f_\varepsilon(r) \tag{23}$$

where γ_1 = liquid–solid interfacial tension and γ_2 = air–solid interfacial tension. The difference between the two terms on the right-hand side of Eq. 22 has been decomposed into two components in Eq. 23: a constant $\Delta\sigma_o$ and a variable component $f_\varepsilon(r)$. In this study, $\Delta\sigma_o$ is written in terms of the static contact angle inside the circular pattern θ_{s1} (with lower contact angle), and Eq. 23 can be expressed as

$$\sigma \cos\theta_s(r) = \sigma \cos\theta_{s1} + f_\varepsilon(r) \tag{24}$$

Here, the variable component $f_\varepsilon(r)$ is defined as the defect force (per unit length) which represents the change of wettability/contact angle across the surface. The defect refers to the chemical heterogeneity of a surface. Substituting Eq. 21 into Eq. 24 yields

$$\sigma(\cos\theta_{s1} - \cos\theta_a) = \beta v_{cl} - f_\varepsilon(r) \tag{25}$$

Equation 25 shows that the out-of-balance surface tension is dissipated in two different channels if the droplet is spreading on a heterogeneous surface. The first term on the right-hand side of Eq. 25 is the energy dissipation in the interfacial region due to adsorption/

desorption on a homogeneous surface, while the second term represents the additional dissipation due to the effect of heterogeneity on the surface. The latter reduces the maximum spread diameter on a surface with heterogeneous wettability which is demonstrated in the simulation, as the DCA tends to its static value. According to Eq. 24, the defect force (which is a negative value in this study) increases in magnitude when the wettability contrast between the two surfaces increases. If the defect force is zero, Eq. 25 simply becomes the conventional boundary condition of a homogeneous surface with a constant SCA of θ_{s1}.

3.4.2 Effect of pattern diameter

The boundary condition on the wetted surface is varied to investigate the effect of wettability pattern diameter on droplet spreading. The diameter of the circular pattern is set to various values (40, 55 and 70 μm) which are smaller than the final spread diameter. On a homogenous surface, the final spread diameter of the droplet is 90 μm or 1.65 times of the droplet initial diameter. The wettability contrast is fixed at 70° with SCA of the inner and outer regions set to 50° and 120°, respectively. The simulation results are shown in Fig. 10a.

As the diameter of the circular pattern is reduced, the final diameter of the droplet reduces accordingly as droplet spreading is confined by wettability contrast. Hence, the final spread diameter is linearly proportional to the diameter of heterogeneous pattern (see Fig. 10a). However, this linear relationship is not obeyed when the diameter of the circular pattern is reduced below a certain threshold. From Fig. 10b, it can be observed that when the diameter of the heterogeneous pattern is reduced to 0.86 times of the droplet diameter or smaller, the final spread diameter does not reduce further. In fact, the threshold diameter of the wettability confinement is the final spread diameter of a droplet on a homogeneous surface with the same contact angle as the outer region. In this case, the final spread diameter on a homogeneous surface with a contact angle of 120° is 0.86D. If D_h* is smaller than 0.86D, the impinging droplet behaves as if the surface is homogeneous due to a lack of interaction between the contact line and the boundary between the two regions with an abrupt change in contact angle. Similar argument applies if D_h* is larger than 1.65D which is the final droplet spread diameter on a surface with a contact angle of 50°.

3.4.3 Effect of impact velocity

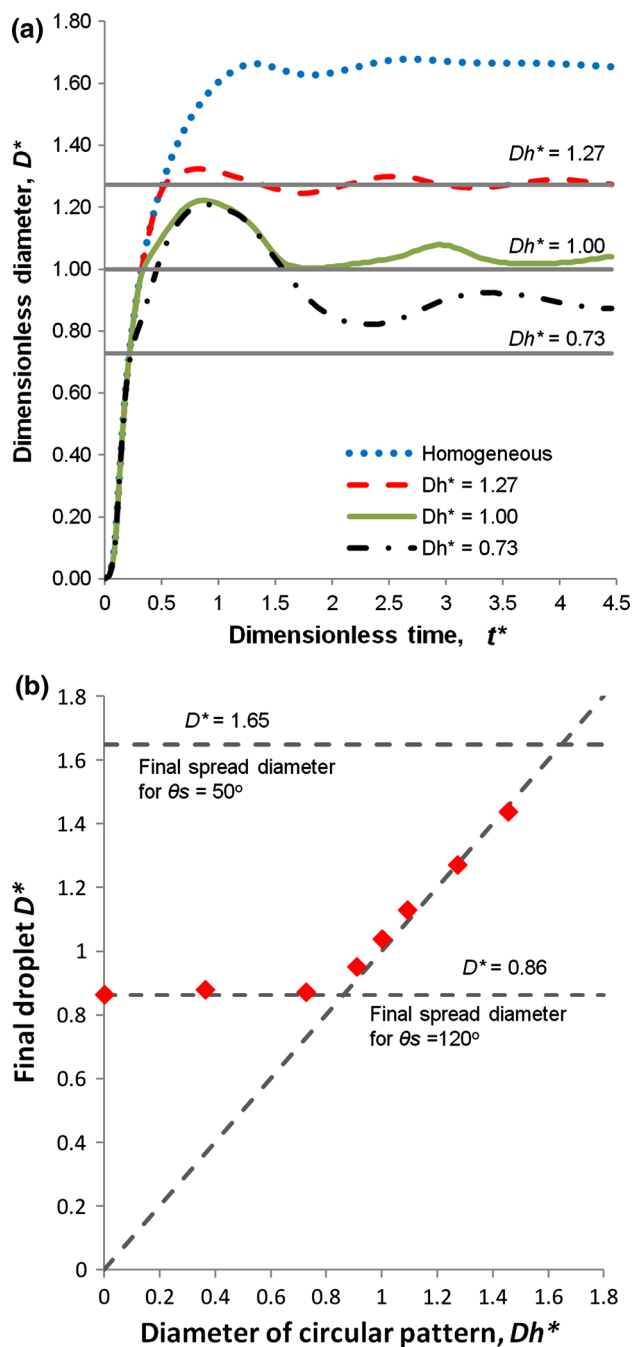The effect of impact velocity on droplet spreading behavior was investigated by varying the droplet impact velocity.

Fig. 10 a Time evolution of droplet spread diameter (non-dimensionalized with droplet initial diameter) upon impingement on a circular pattern with 70° wettability contrast to surrounding surface (SCA of inner and outer regions are 50° and 120°, respectively). Diameter of the circular area is varied. Only selected results are shown for clarity. *Horizontal lines* indicate diameter of circular pattern D_h*. Droplet initial diameter $D = 55$ μm; impact velocity $U = 2.45$ m s^{-1}; We = 4.5; dimensionless time $t* = tU/D$. **b** Final droplet spread diameter on surface with different D_h*. Two *horizontal lines* indicate final $D*$ for homogenous surface with SCA of 50° and 120°, respectively
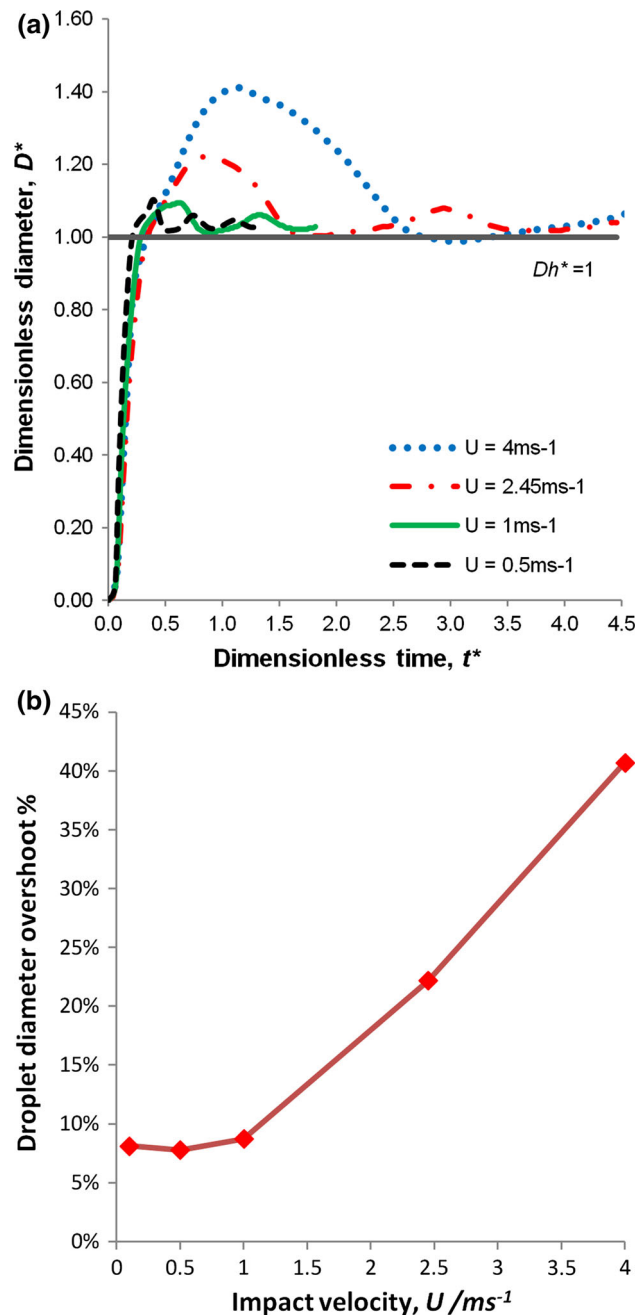
(a)

(b)

Fig. 11 **a** Time evolution of droplet spread diameter (non-dimensionalized with droplet initial diameter) upon impingement on a circular area with 70° wettability contrast to surrounding surface (SCA of inner and outer regions are 50° and 120°, respectively). Droplet impact velocity U is varied; We = 0.19, 0.76, 4.5 and 12. *Horizontal lines* indicate diameter of circular area D_h*. Droplet initial diameter D = 55 μm. Dimensionless time $t* = tU/D$. **b** Overshoot % with different impact velocities
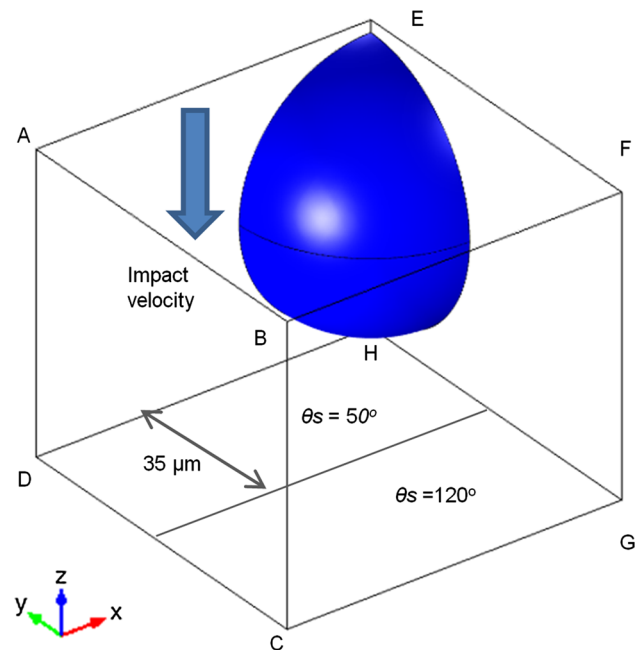

Fig. 12 3D simulation domain for droplet impinging and spreading on striped pattern with wettability contrast. Only a quarter of the droplet is simulated with surface AEHD and EFGH as planes of symmetry; surface CDHG is wetted surface; the other surfaces are open boundaries. Droplet initial diameter D = 55 μm; impact velocity U = 2.45 m s^{-1}; We = 4.5

from 0.19 to 12. Therefore, the velocities are realistic estimates of impact velocity for a DOD inkjet dispenser. The lowest velocity (0.5 m s^{-1}) is meant to illustrate the effect of low impact velocity on the spreading behavior and serves as a comparison for the results at higher impact velocities. The simulated time evolution of the spreading diameter is shown in Fig. 11. At the early stages of droplet impingement, the spreading of droplet is governed by the impact velocity and initial diameter only (Rioboo et al. 2002). Higher impact velocity provides higher kinetic energy for the spreading of the droplet, resulting in larger maximum spread diameter. This causes a higher overshoot from the area of confinement with increasing impact velocity.

After reaching the maximum diameter, the droplet contact line recedes back to the boundary with wettability contrast and the droplet exhibits some oscillations near the boundary before reaching its equilibrium state. The final spread diameters of all droplets are the same regardless of impact velocities. This is because after the kinetic energy is depleted during the initial inertial-dominated spreading, the contact line movement is governed by surface tension and the wetted surface condition. The fluid properties and the surface condition in this series of simulations are the same. In this case of a surface with a single circular pattern of heterogeneity, the minimization of energy brings the
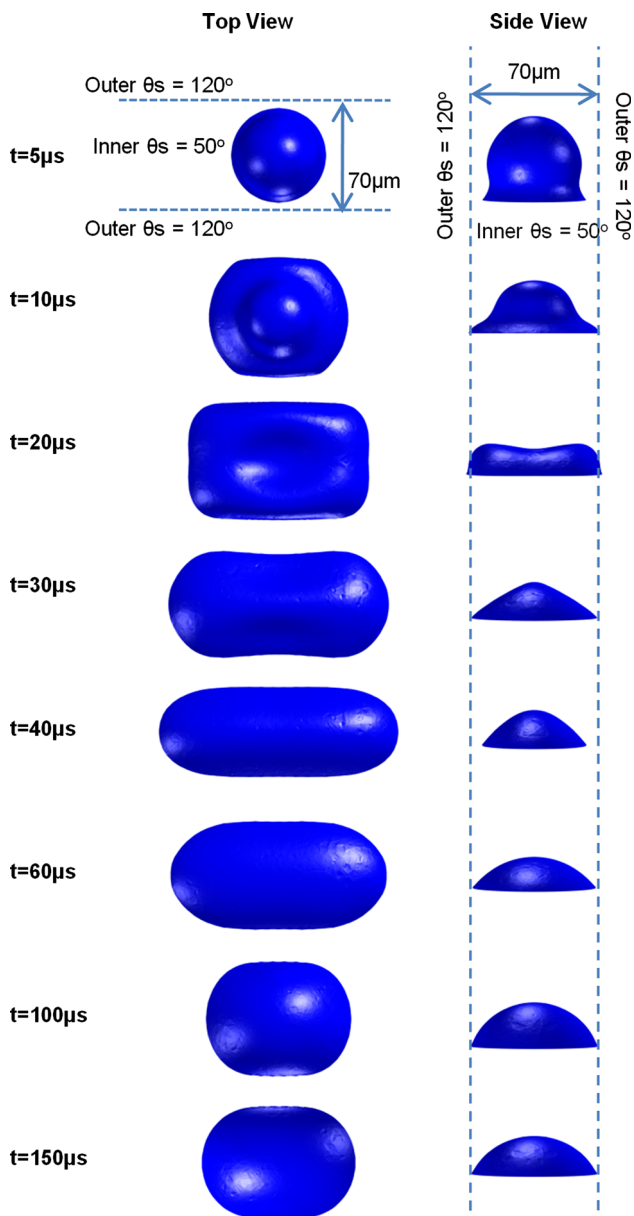
The diameter of the inner circular area is set to the droplet initial diameter ($D_h* = 1$). Droplet impact velocities for a typical drop-on-demand (DOD) inkjet dispenser are 1–8 m s^{-1} (Briones et al. 2010). The impact velocities in our studies are 0.5, 1, 2.45 and 4 m s^{-1} with We ranging

Fig. 13 Top and side views of 55-μm-diameter droplet impinging on a striped pattern (width = 70 μm) with wettability contrast of 70° to surrounding surface. Impact velocity = 2.45 m s^{-1}. We = 4.5
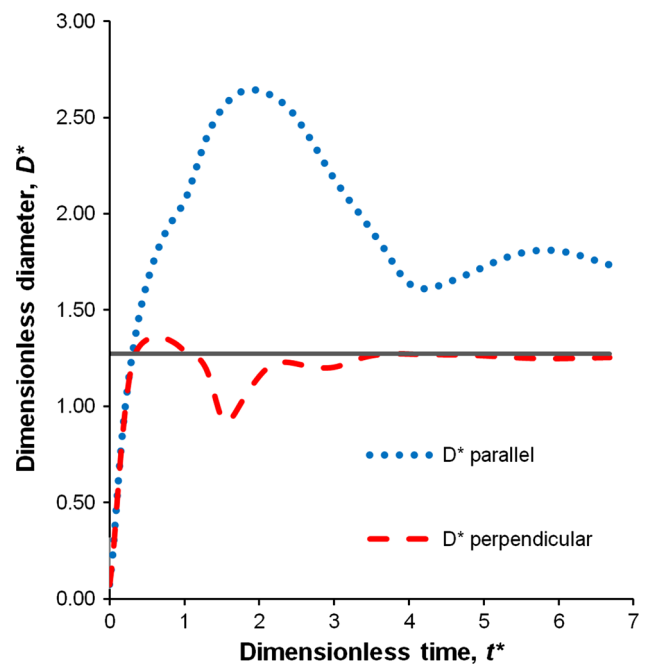

Fig. 14 Time evolution of droplet spread diameter upon impingement on a striped pattern with 70° wettability contrast to surrounding surface (SCA of inner and outer regions are 50° and 120°, respectively). *Horizontal line* indicates stripe width of 70 μm (1.27D). Droplet initial diameter $D = 55$ μm; impact velocity $U = 2.45$ m s^{-1}; $We = 4.5$. Dimensionless time $t^* = tU/D$

droplet back into the circular region with a lower contact angle.

3.5 Impact and spreading on stripe pattern with wettability contrast

The simulation of a droplet impinging on a stripe pattern with a higher wettability than the surrounding surface was performed (see Fig. 12). For 3-dimensional (3D) phase-field simulations, the contact-line-tracking scheme proposed in Sect. 3.2 cannot be applied because the contact line moves in a plane instead on a line. A more complex formulation of the scheme which takes into consideration the change in phase-field gradient in both the x and y directions is required. However, this is not pursued in this study due to limited computation resources. Therefore, static contact angle boundary condition was applied at the surface as an approximation, and the results were compared with results obtained with axisymmetry SCA simulation performed in Sect. 3.3. Due to the large memory required and long computation time, the mesh employed in this 3D simulation is coarser than the axisymmetry case. The smallest mesh size on the surface is set to 4 μm, and the interfacial thickness ε is set to 2 μm accordingly. According to Fig. 2, the simulation result based on this mesh size would still give a good approximation to the results obtained from a finer mesh if κ is set to a value larger than 1.10×10^{-10} m^3 s kg^{-1}.

In the simulation, a droplet with 55 μm diameter impinges on an infinitely long stripe with a width of 70 μm at an impact velocity of 2.45 m s^{-1}. The contact angles inside and outside of the stripe are 50° and 120°, respectively (see Figs. 12, 13). Only a quarter of the droplet was simulated due to symmetry. The full droplet is generated by mirroring the obtained simulation result at the two planes of symmetry. To show the anisotropic spreading behavior of the droplet, the droplet spread length in the parallel and perpendicular directions to the stripe are

plotted in Fig. 14. The spreading of the droplet perpendicular to the stripe is constrained to $1.27D$ by the wettability contrast and is smaller than the equilibrium droplet diameter on a homogeneous surface with SCA of 50° ($1.65D$). Due to mass conservation, the droplet is forced to spread along the direction parallel to the stripe. The maximum spread length along the strip is $2.6D$ and is larger than the maximum droplet spread diameter on a homogeneous surface with SCA of 50° ($2.1D$). This resulted in an elongated droplet in the direction of the stripe pattern.

4 Conclusions

The impingement and spreading of a micro-sized droplet with nonzero impact velocities on a solid surface were modeled numerically based on phase-field method through FEM. Numerical results based on static contact angle and dynamic contact angle boundary conditions were compared. A simple scheme was proposed to track the contact-line velocity which is required to prescribe the boundary condition for dynamic contact angle. The numerical results were verified with experimental results from the literature. Boundary condition of the wetted surface prescribed according to molecular–kinetic theory (Blake's formulation) was found to provide the best fit to the experimental results with physically reasonable parameters, as compared to static contact angle boundary condition or hydrodynamic dynamic contact angle boundary condition.

The model was used to simulate the impingement and spreading of a droplet on a heterogeneous surface. For a circular pattern with a lower contact angle than the surrounding surface, the droplet final spread diameter decreases with increasing wettability contrast. High wettability contrast confines the droplet within the circular area. Decreasing diameter of the circular pattern with high wettability contrast reduces the final droplet spread diameter as the droplet conforms to the pattern. However, the diameter of the droplet cannot be reduced below a certain threshold, which is dictated by the final spread diameter of the droplet on a homogeneous surface with similar contact angle as the outer region of the circle. The droplet maximum spread diameter is larger at higher impact velocities. However, the final droplet diameter is independent of the impact velocity, as the droplet contact line recedes back into the circular pattern after it reaches its maximum diameter.

Impingement and spreading of a droplet on a long stripe pattern with a lower contact angle than the surrounding surface has been demonstrated in a 3D phase-field simulation. With a high wettability contrast between the inner and outer regions of the stripe, the droplet exhibits anisotropic spreading, with a longer spreading length in the direction parallel to the stripe and a smaller spreading length in the direction perpendicular to the stripe. This results in an elongated droplet in the direction of the stripe. These simulations demonstrated that a jetted droplet which impinges on a solid surface can be confined to a selected area through surface wettability patterning.

References

Arias AC, Ready SE, Lujan R, Wong WS, Paul KE, Salleo A, Chabinyc ML, Apte R, Street RA, Wu Y, Liu P, Ong B (2004) All jet-printed polymer thin-film transistor active-matrix backplanes. Appl Phys Lett 85(15):3304–3306

Bhardwaj R, Attinger D (2008) Non-isothermal wetting during impact of millimeter-size water drop on a flat substrate: numerical investigation and comparison with high-speed visualization experiments. Int J Heat Fluid Flow 29(5):1422–1435

Blake TD (2006) The physics of moving wetting lines. J Colloid Interface Sci 299(1):1–13

Blake TD (2012) Forced wetting of a reactive surface. Adv Colloid Interface Sci 179–182:22–28

Blake TD, De Coninck J (2002) The influence of solid–liquid interactions on dynamic wetting. Adv Colloid Interface Sci 96(1–3):21–36

Blake TD, Clarke A, De Coninck J, de Ruijter MJ (1997) Contact angle relaxation during droplet spreading: comparison between molecular kinetic theory and molecular dynamics. Langmuir 13(7):2164–2166

Bliznyuk O, Vereshchagina E, Kooij ES, Poelsema B (2009) Scaling of anisotropic droplet shapes on chemically stripe-patterned surfaces. Phys Rev E 79(4):041601

Bliznyuk O, Jansen HP, Kooij ES, Poelsema B (2010) Initial spreading kinetics of high-viscosity droplets on anisotropic surfaces. Langmuir 26(9):6328–6334

Bliznyuk O, Jansen HP, Kooij ES, Zandvliet HJW, Poelsema B (2011) Smart design of stripe-patterned gradient surfaces to control droplet motion. Langmuir 27(17):11238–11245

Brandon S, Wachs A, Marmur A (1997) Simulated contact angle hysteresis of a three-dimensional drop on a chemically heterogeneous surface: a numerical example. J Colloid Interface Sci 191(1):110–116

Briones AM, Ervin JS, Putnam SA, Byrd LW, Gschwender L (2010) Micrometer-sized water droplet impingement dynamics and evaporation on a flat dry surface. Langmuir 26(16):13272–13286

Brochard-Wyart F, de Gennes PG (1992) Dynamics of partial wetting. Adv Colloid Interface Sci 39:1–11

Cassie ABD, Baxter S (1944) Wettability of porous surfaces. Trans Faraday Soc 40:546–551

Chaudhury MK, Whitesides GM (1992) How to make water run uphill. Science 256(5063):1539–1541

Chu K-H, Xiao R, Wang EN (2010) Uni-directional liquid spreading on asymmetric nanostructured surfaces. Nat Mater 9(5):413–417

Cox RG (1986) The dynamics of the spreading of liquids on a solid surface. Part 1. Viscous flow. J Fluid Mech 168:169–194

de Gennes PG (1985) Wetting: statics and dynamics. Rev Mod Phys 57(3):827–863

Fujimoto H, Shiotani Y, Tong AY, Hama T, Takuda H (2007) Three-dimensional numerical analysis of the deformation behavior of

droplets impinging onto a solid substrate. Int J Multiph Flow 33(3):317–332

Ganesan S (2013) On the dynamic contact angle in simulation of impinging droplets with sharp interface methods. Microfluid Nanofluidics 14(3–4):615–625

Haskal EI, Büchel M, Duineveld PC, Sempel A, Van de Weijer P (2002) Passive-matrix polymer light-emitting displays. MRS Bull 27(11):864–869

Heller MJ (2002) DNA microarray technology: devices, systems, and applications. Annu Rev Biomed Eng 4(1):129–153

Hendriks CE, Smith PJ, Perelaer J, van den Berg AMJ, Schubert US (2008) "Invisible" silver tracks produced by combining hot-embossing and inkjet printing. Adv Funct Mater 18(7):1031–1038

Hutchings MI, Martin DG (2013) Inkjet technology for digital fabrication. John Wiley & Sons Ltd., United Kingdom

Jacqmin D (1999) Calculation of two-phase Navier–Stokes flows using phase-field modeling. J Comput Phys 155(1):96–127

Jacqmin D (2000) Contact-line dynamics of a diffuse fluid interface. J Fluid Mech 402:57–88

Jansen HP, Sotthewes K, Ganser C, Teichert C, Zandvliet HJW, Kooij ES (2012) Tuning kinetics to control droplet shapes on chemically striped patterned surfaces. Langmuir 28(37):13137–13142

Joanny JF, Robbins MO (1990) Motion of a contact line on a heterogeneous surface. J Chem Phys 92(5):3206–3212

Jung YC, Bhushan B (2006) Contact angle, adhesion and friction properties of micro-and nanopatterned polymers for superhydrophobicity. Nanotechnology 17(19):4970–4980

Koo HS, Chen M, Pan PC, Chou LT, Wu FM, Chang SJ, Kawai T (2006) Fabrication and chromatic characteristics of the greenish LCD colour-filter layer with nano-particle ink using inkjet printing technique. Displays 27(3):124–129

Kooij ES, Jansen HP, Bliznyuk O, Poelsema B, Zandvliet HJW (2012) Directional wetting on chemically patterned substrates. Colloids Surf A 413:328–333

Kumar A, Goel G, Fehrenbach E, Puniya AK, Singh K (2005) Microarrays: the technology, analysis and application. Eng Life Sci 5(3):215–222

Kusumaatmaja H, Yeomans JM (2007) Modeling contact angle hysteresis on chemically patterned and superhydrophobic surfaces. Langmuir 23(11):6019–6032

Kusumaatmaja H, Vrancken RJ, Bastiaansen CWM, Yeomans JM (2008) Anisotropic drop morphologies on corrugated surfaces. Langmuir 24(14):7299–7308

Kwak G, Lee DW, Kang IS, Yong K (2011) A study on the dynamic behaviors of water droplets impacting nanostructured surfaces. AIP Adv 1(4):042139

Lai J, Sunderland B, Xue J, Yan S, Zhao W, Folkard M, Michael BD, Wang Y (2006) Study on hydrophilicity of polymer surfaces improved by plasma treatment. Appl Surf Sci 252(10):3375–3379

Lee T, Liu L (2010) Lattice Boltzmann simulations of micron-scale drop impact on dry surfaces. J Comput Phys 229(20):8045–8063

Léopoldès J, Bucknall DG (2005) Droplet spreading on microstriped surfaces. J Phys Chem B 109(18):8973–8977

Lin J, Dahlsten P, Pekkanen J, Linden M, Mäntysalo M, Österbacka R (2009) Surface energy patterning for inkjet printing in device fabrication. In: Proceedings of SPIE 7417, San Diego, 2009, p 74171D

Lin Y, Skjetne P, Carlson A (2012) A phase field model for multiphase electro-hydrodynamic flow. Int J Multiph Flow 45:1–11

Liu H, Zhang Y (2010) Phase-field modeling droplet dynamics with soluble surfactants. J Comput Phys 229(24):9166–9187

Lunkad SF, Buwa VV, Nigam KDP (2007) Numerical simulations of drop impact and spreading on horizontal and inclined surfaces. Chem Eng Sci 62(24):7214–7224

Mani M, Mandre S, Brenner MP (2010) Events before droplet splashing on a solid surface. J Fluid Mech 647:163–185

Mei J, Lovell MR, Mickle MH (2005) Formulation and processing of novel conductive solution inks in continuous inkjet printing of 3-D electric circuits. IEEE Trans Electron Packag Manuf 28(3):265–273

Mukherjee S, Abraham J (2007) Investigations of drop impact on dry walls with a lattice-Boltzmann model. J Colloid Interface Sci 312(2):341–354

Raphael E, de Gennes PG (1989) Dynamics of wetting with nonideal surfaces. The single defect problem. J Chem Phys 90(12):7577–7584

Ren W, E W (2011) Contact line dynamics on heterogeneous surfaces. Phys Fluids 23(7):072103

Ren W, Hu D, Weinan E (2010) Continuum models for the contact line problem. Phys Fluids 22(10):102103

Rioboo RR, Marengo MM, Tropea CT (2002) Time evolution of liquid drop impact onto solid, dry surfaces. Exp Fluids 33(1):112–124

Roisman IV, Opfer L, Tropea C, Raessi M, Mostaghimi J, Chandra S (2008) Drop impact onto a dry surface: role of the dynamic contact angle. Colloids Surf A 322(1–3):183–191

Sato Y, Ničeno B (2012) A new contact line treatment for a conservative level set method. J Comput Phys 231(10):3887–3895

Schwartz LW, Eley RR (1998) Simulation of droplet motion on low-energy and heterogeneous surfaces. J Colloid Interface Sci 202(1):173–188

Sele CW, von Werne T, Friend RH, Sirringhaus H (2005) Lithography-free, self-aligned inkjet printing with sub-hundred-nanometer resolution. Adv Mater 17(8):997–1001

Seppecher P (1996) Moving contact lines in the Cahn–Hilliard theory. Int J Eng Sci 34(9):977–992

Seveno D, Ogonowski G, De Coninck J (2004) Liquid coating of moving fiber at the nanoscale. Langmuir 20(19):8385–8390

Seveno D, Vaillant A, Rioboo R, Adão H, Conti J, De Coninck J (2009) Dynamics of wetting revisited. Langmuir 25(22):13034–13044

Seveno D, Blake TD, Goossens S, De Coninck J (2011) Predicting the wetting dynamics of a two-liquid system. Langmuir 27(24):14958–14967

Sirringhaus H, Kawase T, Friend RH, Shimoda T, Inbasekaran M, Wu W, Woo EP (2000) High-resolution inkjet printing of all-polymer transistor circuits. Science 290(5499):2123–2126

Takada N, Tomiyama A (2007) Numerical simulation of isothermal and thermal two-phase flows using phase-field modeling. Int J Mod Phys C 18(04):536–545

Tao Z, Bhushan B (2006) Wetting properties of AFM probes by means of contact angle measurement. J Phys D Appl Phys 39(17):3858

Tekin E, Smith PJ, Schubert US (2008) Inkjet printing as a deposition and patterning tool for polymers and inorganic particles. Soft Matter 4(4):703–713

Ummartyotin S, Juntaro J, Wu C, Sain M, Manuspiya H (2011) Deposition of PEDOT: PSS nanoparticles as a conductive microlayer anode in OLEDs device by desktop inkjet printer. J Nanomater 2011:606714

Voinov OV (1976) Hydrodynamics of wetting. Fluid Dyn 11(5):714–721

Wang JZ, Zheng ZH, Li HW, Huck WTS, Sirringhaus H (2004) Dewetting of conducting polymer inkjet droplets on patterned surfaces. Nat Mater 3(3):171–176

Wang ZK, Zheng HY, Lam YC (2011) Investigation on femtosecond laser irradiation energy in inducing hydrophobic polymer surfaces. Appl Surf Sci 257(24):10427–10433

Wenzel RN (1936) Resistance of solid surfaces to wetting by water. Ind Eng Chem 28(8):988–994

Wörner M (2012) Numerical modeling of multiphase flows in microfluidics and micro process engineering: a review of methods and applications. Microfluid Nanofluidics 12(6): 841–886

Wylock C, Pradas M, Haut B, Colinet P, Kalliadasis S (2012) Disorder-induced hysteresis and nonlocality of contact line motion in chemically heterogeneous microchannels. Phys Fluids 24(3):032108

Xia D, Johnson LM, López GP (2012) Anisotropic wetting surfaces with one-dimesional and directional structures: fabrication approaches, wetting properties and potential applications. Adv Mater 24(10):1287–1302

Xu X, Qian T (2012) Droplet motion in one-component fluids on solid substrates with wettability gradients. Phys Rev E 85(5):051601

Yan YY, Zu YQ (2007) A lattice Boltzmann method for incompressible two-phase flows on partial wetting surface with large density ratio. J Comput Phys 227(1):763–775

Yokoi K, Vadillo D, Hinch J, Hutchings I (2009) Numerical studies of the influence of the dynamic contact angle on a droplet impacting on a dry surface. Phys Fluids 21(7):072102

Yue P, Feng JJ, Liu C, Shen J (2004) A diffuse-interface method for simulating two-phase flows of complex fluids. J Fluid Mech 515:293–317

Yue P, Zhou C, Feng JJ (2010) Sharp-interface limit of the Cahn–Hilliard model for moving contact lines. J Fluid Mech 645:279–294

Zhou C, Yue P, Feng JJ, Ollivier-Gooch CF, Hu HH (2010) 3D phase-field simulations of interfacial dynamics in Newtonian and viscoelastic fluids. J Comput Phys 229(2):498–511